A pyroelectric detector-based method for low uncertainty spectral irradiance and radiance responsivity calibrations in the infrared using tunable lasers

BRIAN G. ALBERDING, JOHN T. WOODWARD IV, PING-SHINE SHAW, LEONARD M. HANSSEN, CATHERINE C. COOKSEY, AND JOSEPH P. RICE

National Institute of Standards and Technology, Sensor Science Division, Gaithersburg, MD, USA
brian.alberding@nist.gov

Abstract: The standard uncertainty of detector-based radiance and irradiance responsivity calibrations in the short-wave infrared (SWIR) traditionally has been limited to around 1 % or higher by the poor spatial uniformity of detectors used to transfer the scale from radiant power. Pyroelectric detectors offer a solution that avoids the spatial uniformity uncertainty, but also introduces additional complications due to alternating current (AC) measurement techniques. Herein, a new method for low uncertainty irradiance responsivity calibrations in the SWIR is presented. An absolute spectral irradiance responsivity scale was placed on two pyroelectric detectors (PED) at wavelengths, λ, from 500 nm to 3400 nm. The total combined uncertainty (k=1) was ≈ 0.28 % (> 1000 nm), 0.44 % (900 nm), and 0.36 % (≈ 950 nm and < 900 nm) for PED #1 and 0.34 % (> 1000 nm), 0.48 % (900 nm), and 0.42 % (≈ 950 nm and < 900 nm) for PED #2. This was done by utilizing a demodulation technique to digitally analyze the time-dependent, AC, waveforms, which obviates the use of lock-in amplifiers and avoids associated additional uncertainty components.

1. Introduction

Absolute radiometric measurements are important for a wide range of applications within defined spectral regions [1,2]. Associated uncertainties are extremely important as measurements from space-based remote sensing instruments, for example, can occur over a long-time scale (tens of years) [3]. Lower uncertainties mean that trends in data products can be determined in shorter periods of time [4]. Ultimately, these data products rely on reference measurements and calibration scales to determine the measurand of interest, typically radiance or irradiance, with high accuracy and precision. Historically, the lowest uncertainty measurements occur in the visible where high-quality silicon transmission trap detectors are available as reference standards. Lowering of the uncertainty to equivalent levels in the short-wave infrared has proven more problematic.

A method for calibrating instruments directly in irradiance or radiance mode using high power, narrow bandwidth lasers and has achieved low uncertainty at the ≈ 0.1 % level or less. At National Institute of Standards and Technology (NIST) the facility for this is called SIRCUS (Spectral Irradiance and Radiance Calibrations using Uniform Sources) [5–7]. Low uncertainties are achieved by traceability to the NIST Primary Optical Watt Radiometer (POWR) [8] and the NIST Aperture Area Measurement Facility [9]. In short, a transfer standard silicon trap detector equipped with a precision aperture is calibrated for power responsivity by a cryogenic radiometer with a narrow-band, continuous wave (cw), laser in an underfilled-aperture configuration. Irradiance responsivity, required when the detector is used in an overfilled-aperture configuration, is therefore determined from the measured aperture area. It can then be transferred to other detectors using SIRCUS, where the uncertainty is limited by the uniformity of the transfer detector. This method works well in the silicon detector region, where highly uniform tunnel-trap detectors are available.

In the short-wave infrared (SWIR), Germanium (Ge), indium gallium arsenide (InGaAs), or extended-InGaAs (ex-InGaAs) detectors are typical. These detectors utilize either single-element or trap designs, but do not have sufficient uniformity to do an equivalent transfer with such low uncertainty [10–12]. Sphere detectors have also been used to combat spatial uniformity issues but have additional limitations due to low throughput and scale instability due to sphere degradation [13–15,5]. Pyroelectric detectors offer another potential solution to the spatial uniformity problem where an irradiance scale traceable to POWR in the SWIR can be achieved with uncertainties approaching those obtained in the silicon spectral region.

Fig. 1 depicts the calibration graphically as a function of wavelength and light source beam diameter (left side) and pictorially for overfilled (irradiance) and underfilled (POWR) detector aperture configurations (right side). In the lower left quadrant, a power calibration is conducted in the silicon region on a reference detector using a small diameter laser source. With a precision aperture the *irradiance* responsivity is known from the aperture area, which corresponds to moving up to the top-left quadrant in Fig. 1, and the uncertainty depends on the detector non-uniformity. The same process can be repeated for InGaAs or ex-InGaAs detectors (Fig. 1, left, above 900 nm), except none exist with non-uniformity low enough to allow 0.1 % level uncertainties as is the case in the silicon range with tunnel-trap detectors.

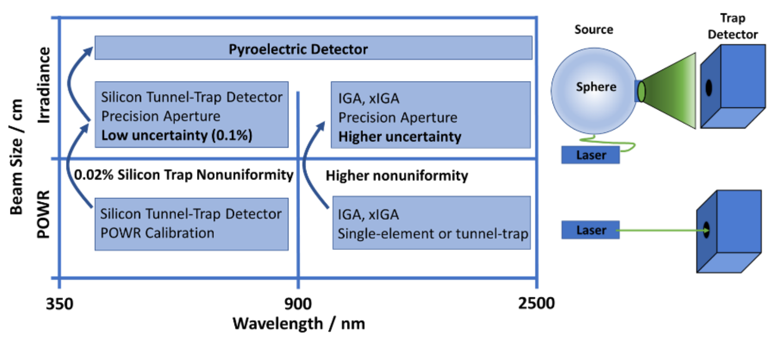

Fig. 1. Representation of responsivity calibration as a function of source beam size (Y-axis) and wavelength (X-axis) along with a depiction of the illumination geometry (right-side).

Several features of pyroelectric detectors allow circumvention of the detector non-uniformity problem. One, being thermal detectors, black-coated pyroelectric detectors have power or irradiance responsivity that is nearly spectrally flat [16]. Measurement of the spectral absorptance yields an independent determination of the responsivity curve. Two, the absorptive black coatings have low reflectance and negligible transmission. Therefore, the relative spectral responsivity is proportional to the relative spectral absorptance, which in turn can be determined by $A(\lambda) = 1 - R(\lambda) - T(\lambda)$, where $R(\lambda)$, $T(\lambda)$, and $A(\lambda)$ are the wavelength (λ) dependent reflectance, transmittance, and absorptance, respectively. Three, the broadband responsivity allows an irradiance responsivity scale transfer (at the SIRCUS facility, top left arrow in Fig. 1) against a silicon tunnel trap detector at one or more tie point wavelengths. Using the tie point absolute irradiance responsivity, the absorptance curve $A(\lambda)$ provides the relative spectral part of the absolute spectral irradiance responsivity scale across its entire measured wavelength range.

Use of the pyroelectric detector circumvents problems with detector non-uniformity but also requires modifications from the usual calibration technique. Foremost, it requires use of an optical chopper to generate an alternating current (AC) signal. This is usually combined with use of a lock-in amplifier to analyze the quasi-square wave signal. However, use of a lock-in amplifier also confounds the calibration because the measured signal is not the peak-to-peak signal of the input quasi-square waveform (i.e. is not equivalent to the direct current (DC) signal, which is needed for absolute radiometric measurements) but instead is only derived from the amplitude of the first sine component [17]. The measured lock-in amplifier signal (which is root mean square voltage, V_{rms}) requires a factor of about 0.45 to return the peak-to-peak signal but for low uncertainty requires independent calibration and adds an additional step to the overall calibration chain. Furthermore, transient features in the waveform signal, such as detector rise times or power stabilizer settling times, will cause additional errors that are dependent on specific experimental configurations. Lastly, multiple lock-in amplifiers would be needed to complete the calibration for the detector under test (DUT), reference, and the monitor signals. Instead of a lock-in amplifier, a digital-to-analog converter can be used to collect and process the entire time-dependent waveform. In this way, the waveform can be directly analyzed to remove unwanted transient features and directly measure the peak-to-peak, DC, signals.

Pyroelectric detectors have been previously used for similar calibration methods using monochromator-based light sources [18]. Two significant advancements are reported for laser-based methods. One, an irradiance responsivity calibration scale is established in the SWIR on a pyroelectric detector with low uncertainty approaching that which is possible in the silicon range using laser-based sources. This is done by measuring the directional-hemispherical reflectance of a *witness sample* detector and performing an irradiance responsivity calibration on a *real* detector at selected tie points against a silicon tunnel trap detector. Two, the pyroelectric detector signal is utilized in chopped, AC mode, without using a lock-in amplifier.

2. Experimental[a]

2.1 Pyroelectric detectors and witness sample

The pyroelectric detectors (PED #1 and PED #2) were both purchased from a commercial source (Gentec-eo Model SDX-1005) but were manufactured from separate batches. Each detector has an internal current-to-voltage converter that operates at a fixed gain and has a 5 mm diameter active area. The detectors were equipped with a circular aperture having a nominal area of 9.62 mm^2 and an SM1 lens tube with 1.27 cm length. Black spray paint was used to coat the lens tube and reduce internal reflections.

The witness detector consisted of a 9 mm diameter pyroelectric "detector" specifically manufactured as a witness sample in an identical manner and as part of the same batch as PED #1. It has the same black coating on the same type of pyroelectric element with the same gold coating on the back of the detector element but is mounted in its housing in a way that provides complete hemispherical access to the front surface, enabling it to be placed optimally against an integrating sphere for complete collection of the diffuse reflected light. It has no electrical connections and so is not a real detector but is otherwise optically identical to a real detector. There were two such witness sample detectors. Photographs of a witness sample detector along with the actual detectors PED #1 and PED #2 are shown in the supporting information, Fig. S1

2.2 Reflectance Measurements

Reflectance measurements of the pyroelectric detector witness samples were performed in two wavelength ranges; from 500 nm to 2500 nm (VNIR) and from 800 nm to 3400 nm (SWIR) using separate instruments (See supporting information, Fig. S2, for raw data scans). Spectral directional hemispherical reflectance was measured in both ranges. For the former range a spectrophotometer was used with an Integrating Sphere Assembly operating in reflectance

[a] Certain commercial equipment or materials are identified in this paper to adequately specify the experimental procedures. In no case does the identification imply recommendation or endorsement by NIST, nor does it imply that the materials or equipment identified are necessarily the best available for the purpose.

mode [19,20]. This measurement included any specular components of the reflectance. Each witness sample detector was spectrally scanned multiple times and averaged. For the latter range, a Fourier transform spectrometer was used in near-infrared (NIR) mode with a resolution of 16 cm^{-1} [21,22]. Each witness sample was measured on two occasions and on each occasion the measurement was repeated 30 times over 4 h and averaged. Specular components to the reflectance were found to be negligible within the expanded uncertainty via a separate measurement. The final reflectance spectrum $R(\lambda)$ was obtained by combining the results from the VNIR and SWIR measurements at 1000 nm and averaging the spectra from the two witness samples. This spectrum was then converted to absorptance using $A(\lambda) = 1 - R(\lambda) - T(\lambda)$, with $T(\lambda) = 0$, and fit to a sigmoidal function.

2.3 SIRCUS method

The NIST SIRCUS facility has been described previously [5,6]. Briefly**,** the system consists of a Lambertian source generated by coupling a tunable laser to an integrating sphere (12-inch diameter, Spectralon coated, with a 2-inch diameter aperture) via an optical fiber. A detector-based substitution method is used, typically in DC mode using an optical shutter for signal and background measurements. First, the irradiance of the source is measured using a reference detector. Then, the source is observed by the device under test (DUT) to determine its irradiance (or, by a geometric factor, radiance) responsivity. In each case, the detector measurement planes were aligned with the source aperture plane by back-reflection of an alignment laser. Inverse square law measurements allow for the irradiance of the source to be known at the DUT reference plane by determination of the detector positions.

In the wavelength range 350 nm to 900 nm, the reference detector is a silicon tunnel-trap detector that has been calibrated by the NIST Primary Optical Watt Radiometer (POWR) [8] for power responsivity in an under-filled configuration and equipped with a precision aperture calibrated by the NIST aperture area facility [9]. Each measurement is also ratioed to a corresponding measurement of a monitor photodiode directly mounted to the sphere to account for any radiant flux changes between measurements. Finally, the laser system also consists of components for measuring the wavelength with a wavemeter (with 0.005 nm accuracy and 0.001 nm resolution), power stabilization (5 kHz bandwidth with 200:1 noise reduction at 1 Hz and 0.03 % long-term stability), fiber coupling, and speckle reduction (utilizing a bare fiber patch cable submerged in a sonicator bath modulated at 20 kHz). A set of continuous wave lasers (dye laser and a home-built titanium:sapphire laser) were used to cover the wavelength range for measuring the irradiance responsivity of the pyroelectric detectors at the various tie points.

Two changes have been made to accommodate use of the pyroelectric detector with chopped source modulation. First, a chopper was added to the optical laser path to generate a pulsed, AC, waveform signal. The signal was chopped at 10 Hz modulation frequency, well below the 3 dB responsivity roll-off at 100 Hz for the pyroelectric detector [23]. Modulation frequencies of 10.5 Hz or 9 Hz did not yield significantly different results. Second, data was acquired using a multifunction I/O device (National Instruments model NI USB-6211) with an analog-to-digital converter (ADC) with 16-bit resolution and 250 kHz maximum sampling rate. Signals from the detector (reference or DUT), monitor photodiode, and chopper reference were simultaneously recorded into separate analog input channels as the time-dependent waveform. The waveforms were then demodulated using a digital signal processing algorithm in real time (see Results, Section B, below) to determine the response of each detector. Note that lock-in amplifiers were avoided in this last step since that would have led to additional uncertainties associated with the non-ideal square wave shape of the waveforms.

2.4 Inverse square law measurements

At several different Z-positions of the integrating sphere source along the optical axis, the detector and monitor voltages were recorded to yield a relative irradiance for the reference trap and DUTs (pyroelectric detectors). The extended-source version of the $1/Z^2$ law for on-axis irradiance (inverse square law) was fit to the resultant data to yield the Z-position of the detector aperture plane. From the Z-position encoder reading used in the irradiance calibration measurements and the detector Z-position of the detector from the radiometric $1/Z^2$ law fit, the actual detector measurement plane to sphere aperture distance in millimeters was determined for the DUT and reference detectors.

2.5 Data Acquisition and Analysis

Irradiance data was acquired using an automation program to control the position of the integrating sphere source on an XYZ translation stage and record detector signals from the ADC. Each detector (DUT or reference) was aligned sequentially to the optical axis of the integrating sphere using the motorized XY translation. The time-dependent waveforms of the chopped signals from the detectors were measured by the ADC module, along with the simultaneously recorded monitor signal, in separate analog input channels (differential mode). The data was demodulated after each square waveform collection to give the DC signal as the difference between the average peak and valley signals for each cycle in the waveform for both the detector and the monitor, after removal of any transient features, to generate a nearly ideal square waveform. This resulted in an array of DC signals for both the DUT and monitor, which were then ratioed. The chopping frequency was 10 Hz while the data acquisition was completed at 10 kHz sampling rate. Note that the analysis method results in rejection of 1 cycle in the waveform as explained in more detail in Section 3.2, below.

Statistics for the measured ratio (DUT/monitor) were determined from the number of cycles in a single waveform collection or by repeating several short waveform collections. For the irradiance responsivity measurements of the pyroelectric detectors, waveforms of 10 s duration were collected and repeated 180 times to yield the average ratio and percent standard deviation of the mean. For the inverse square law measurements, the number of repeats was varied depending on the measured signal magnitude ranging from 9 repeats to 150 repeats when the sphere was at the largest distance position. Scans for the reference trap detector were repeated 10 times, where fewer repeats were required to achieve the desired measurement standard deviation due to the higher signal-to-noise possible with this detector.

3. Results and Discussion

The calibration chain to determine the pyroelectric detector irradiance responsivity in the SWIR from approximately 500 nm to 3400 nm is shown in Figure 2. The calibration consisted of combining two independent sets of measurements. Reflectance measurements of the witness sample detectors determined the relative spectral responsivity, via the absorptance, over the entire spectral range of interest. SIRCUS calibrations then set the absolute irradiance responsivity scale. First, a reference standard silicon tunnel-trap detector with a high-precision aperture was directly calibrated by the NIST POWR in an underfilled configuration (radiant power responsivity, Fig. 2, Step 1). The spatial uniformity of the silicon tunnel-trap detector and the measured aperture area enables this detector to serve as an irradiance reference standard at SIRCUS, as is usual [5,6]. Next, the pyroelectric detectors were calibrated on SIRCUS in overfilled mode (irradiance responsivity, Fig. 2, Step 2a) against the reference standard silicon detector at several tie points (600 nm to 900 nm) within the silicon detector responsivity range. Finally, these pyroelectric detector absolute irradiance responsivity measurements were used to tie the relative spectral irradiance over the full spectral range to the absolute irradiance responsivity scale (Fig. 2, Step 3). Details of these steps in the calibration chain follow.

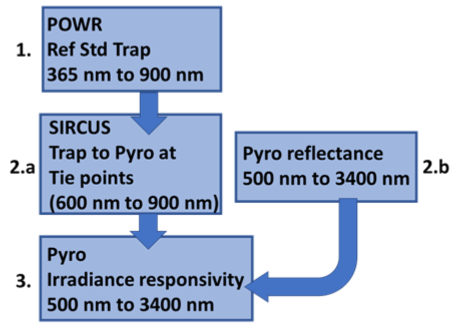

Fig 2. Block diagram of the calibration chain for the irradiance responsivity scale of the two pyroelectric detectors in the SWIR spectral range.

3.1 Witness Sample Reflectance

Directional hemispherical diffuse reflectance and specular reflectance were measured for the two witness sample pyroelectric detectors in the range 500 nm to 3400 nm (Fig. S2, supporting information). Two separate instruments were used to cover the full spectral range, and the spectra were combined at 1000 nm. A single curve was then obtained by averaging the spectra for the two witness samples. Fig. 3 (bottom) shows the absorptance spectrum determined this way and by using equation 1, where the transmittance was negligible.

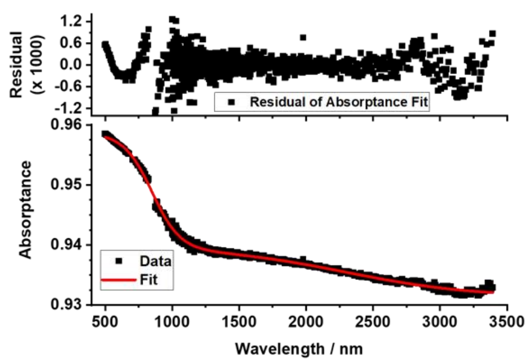

Fig 3. Fit of a double (2 term) sigmoidal function (Equation 1) to the absorptance data of the pyroelectric detector witness sample (bottom) along with the residuals of the fit scaled by a factor of 1000 (top).

Towards generating a smooth standard irradiance responsivity curve in the SWIR, a fitting analysis was completed for the witness sample absorptance spectra. Several fitting functions were considered, including multi-order polynomial, multi-peak Gaussian, and a sigmoidal function. All three types produced reasonable results with a coefficient of determination (R^2) greater than 0.99 but significant deviations were observed at the edges of the spectrum and the former two functions required an inordinate number of terms. Additionally, the multi-peak fitting analysis failed to converge and was not reproducible due to arbitrary selection of peak positions. Ultimately, the broad featureless nature of the reflectance spectrum worked well with the double sigmoidal type (bi-dose response) function shown in equation 1, where A_1, A_2, p, h_1, h_2, $x_{0,1}$ and $x_{0,2}$ are fitting parameters, y is the absorptance, and x is the wavelength.

$$y = A_1 + (A_2 - A_1)\left[\frac{p}{1 + 10^{(x_{0,1}-x)h_1}} + \frac{1-p}{1 + 10^{(x_{0,2}-x)h_2}}\right] \quad (1)$$

The results of the sigmoidal fit to the absorptance spectra data are shown in Table 1 as well as in Figure 3 as the solid red line (bottom) and fit residuals (top). Aside from the slight deviations below 800 nm and above 3300 nm the sigmoidal function fit quite well across the spectral range and through the shoulder region at 1000 nm. Despite the slight deviations, the residuals are all below 0.12 %. A histogram shows the residuals are less than 0.1 % for 99 % of the points and less than 0.05 % for 90 % of the points (see supporting information Fig. S3). Most importantly, the region above ≈ 1000 nm, where silicon detectors have limited usefulness, clearly shows residuals at less than the 0.1 % level, which is a target for achieving uncertainty competitive with typical irradiance responsivity measurement techniques in the silicon range. The fit also allows a smooth curve to be generated, where the measurement noise and fit residuals are folded in as an uncertainty component to the irradiance responsivity curve, as described below.

Table 1: Results of the fit of equation 2 to the witness sample pyroelectric detector absorptance data

A_1	$0.93131 \pm 1.5\text{x}10^{-4}$
A_2	$0.95878 \pm 1.0\text{x}10^{-4}$
$x_{0,1}$	849.3 ± 1.9 nm
$x_{0,2}$	2298 ± 15 nm
h_1	$-0.00414 \pm 5\text{x}10^{-5}$ / nm
h_2	$-9.1\text{x}10^{-4} \pm 4\text{x}10^{-5}$ / nm
p	0.696 ± 0.008
Reduced Chi-Squared	$9.6\text{x}10^{-8}$
R^2	0.996

3.2 Irradiance Data Acquisition and Analysis

Irradiance responsivity measurements were made in SIRCUS for the pyroelectric detectors (PED #1 and PED #2) using the silicon tunnel trap detector as the reference standard. A silicon photodiode was used as a monitor detector on the SIRCUS integrating sphere, as usual. Examples of the raw data waveforms are shown in Fig. 4. The top panel of Fig. 4 shows an expanded view of the waveform for the reference detector and the simultaneously recorded sphere monitor detector. Here, typical time-dependent effects can be observed. The spike on the falling edge of the monitor curve arises due to power stabilization (where the monitor signal is used in the feedback control loop) and the effects of detector pre-amplifier time-constants can be clearly seen in the rising and falling edges of the red curve. Even though speckle reduction techniques are used during the measurement, slight oscillations are also observed.

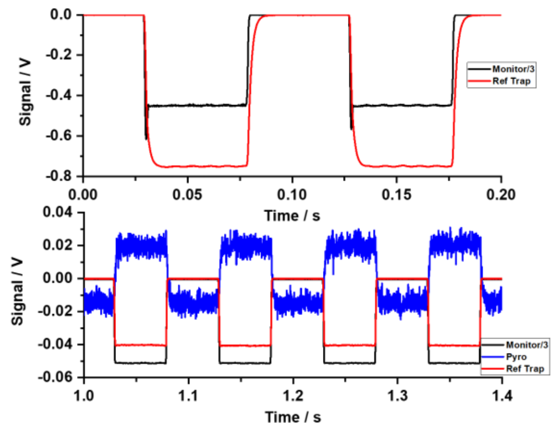

Fig. 4. Representative 10 Hz waveform responses of the irradiance at ≈ 715 nm as measured by the silicon trap and one pyroelectric detector using the ADC at an acquisition rate of 10 kHz. Top: trap (red) and monitor photodiode (black) detector waveforms showing transient and temporal effects such as power stabilization, time constant and speckle. Bottom: Typical waveforms collected from the pyroelectric (blue), trap (red), and monitor photodiode (black) detectors in irradiance responsivity measurements.

The bottom panel shows example measurements including the pyroelectric detector under typical conditions, where a power stabilizer wasn't used in this example. A main advantage of using the analog-to-digital converter versus the lock-in amplifier is that the transient regions of the waveform could be removed. This was done by indexing the monitor signal waveform for a threshold value given by the average of the highest and lowest 20 % of values in the waveform array (loop through each value in the monitor waveform array comparing adjacent values to the threshold value. The loop index for which the waveform value is greater than the threshold and the preceding value is less than the threshold gives the index of the threshold value in the rising and falling edges). Index values for the threshold signal were determined only for the monitor but are equivalent for the irradiance detectors as the waveforms are in-phase as shown by Fig. 4. About 15 ms of values on both sides of the threshold index were then removed from each detector waveform to give a pure square wave signal with instantaneous rising and falling edges. Due to the slow drift in the background level of the pyroelectric detector, the DC signal was determined as the difference between the average peak signal and the average signal of the two adjacent valley signals, which results in rejection of 1 cycle of the square waveform signal from the analysis. The DC signals were then ratioed to the simultaneously measured monitor signal for the pyroelectric detector and tunnel-trap reference detector.

Statistics were determined by repeating 10 s duration waveform collections 180 times (30 min collection times). A single long-time waveform collection (several minutes) was also measured, and an Allan variance analysis was completed to show that each cycle provided an independent measurement of the DC signal. Therefore, improved measurement uncertainties were obtained by taking the standard deviation of the mean. Even with the low signal-to-noise exhibited by the pyroelectric detector, the measurement technique could isolate small signals without the use of a lock-in amplifier. The pyroelectric detector signal shown in Fig. 4 has a signal-to-noise of ≈ 4 but signals as small as 1 mV in the ≈ 10 mV noise were possible to detect with reasonable measurement standard deviation of the mean (tenths of a percent) even with short collection times of 1 min or less. It is notable that one major benefit of using a lock-in amplifier is also exhibited by this technique, namely small, modulated, signals can be extracted from high noise, while avoiding absolute calibration related problems associated with use of a lock-in amplifier (i.e. calibration of the lock-in amplifier signal to the DC signal as noted in the introduction section, above).

3.3 Irradiance Measurements

Absolute spectral irradiance responsivity of the pyroelectric detectors, $I_{DUT}(\lambda)$ was determined by the measurement equation, equation 2, where $I_{trap}(\lambda)$ is the known irradiance responsivity of the tunnel-trap detector (in units of A cm^2/W), S_{trap} is the signal measured by the trap of the source irradiance, S_{DUT} is the signal of the pyroelectric detector, and S_{mon} is the sphere monitor signal measured simultaneously with either the trap detector or the pyroelectric detector (DUT) [6]. All measured signals, *S*, are in units of volts and determined from the waveform data as describe above in section B. The pyroelectric detector has an internal amplifier that operates with a fixed gain. Therefore, the irradiance responsivity for the pyroelectric detectors must have units of V cm^2/W and this is converted from the gain setting from the trap transimpedance amplifier, which was 1×10^4 V/A (i.e. $S_{trap}[V] = i_{trap}[A] \times G[V/A]$, where i_{trap} is the trap photocurrent, *G* is the trap transimpedance preamplifier gain, and the units are in the square brackets).

$$I_{DUT}(\lambda) = \frac{I_{Trap}(\lambda)\left(S_{DUT}/S_{Mon,DUT}\right)}{\left(S_{Trap}/S_{Mon,Trap}/G_{trap}\right)CF} \qquad (2)$$

$$CF = \frac{r_s^2 + r_{d,trap}^2 + d_{trap}^2}{r_s^2 + r_{d,trap}^2 + d_{DUT}^2} \qquad (3)$$

The last factor in equation 2, *CF*, is a correction factor that accounts for the difference in the source distance (working distance) for the trap reference detector and DUT detectors (PED #1 and PED #2) [6]. The correction factor *CF*, equation 3, converts the irradiance of the sphere source measured by the trap at the trap reference plane to the irradiance of the sphere source measured by the trap at the DUT reference plane. An extended source geometry is used to calculate the correction factor, where r_s and r_d are the known radii for the source sphere and trap detector apertures, respectively, and *d* is the distance between the source and either the trap detector or DUTs. Under typical conditions the working distances are much greater than the aperture radii, so the correction factor and any associated uncertainty is dominated by the distance.

Working distances were determined radiometrically using the inverse square law for an extended source geometry. These results are shown in Fig. 5 for the reference trap detector and PED #1 (For PED #2 the results are shown in the supporting information, Fig. S4). Here, the irradiance is measured as the signal measured by each detector relative to the simultaneously measured monitor signal (S/S_{mon} as determined from the modulated waveform as described in Section B, above) as a function of the sphere source position. The inverse square law for an extended source geometry is shown in Equation 4, where *y* is the relative irradiance, m_1 is a fitting constant, M_0 is the sphere position (independent variable), m_2 is the position of zero offset for the detector (i.e. the fixed position of the detector on the sphere z-axis translation scale), r_s is the sphere aperture radius, and r_d is the detector aperture radius.

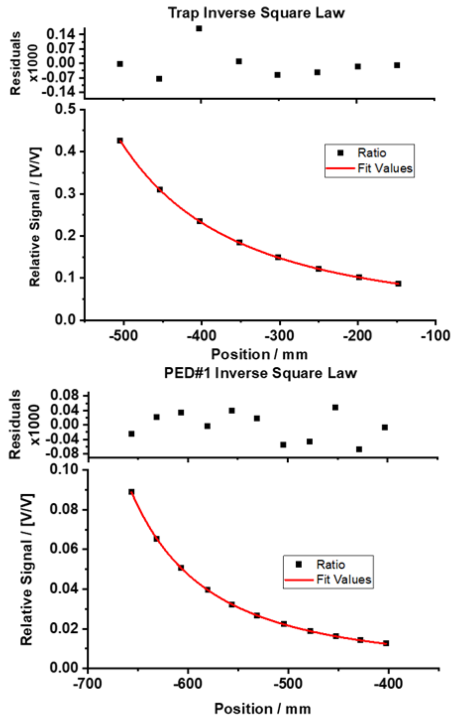

Fig. 5. Inverse square law measurements for the tunnel trap detector (top) and the pyroelectric detector PED #1 (bottom) at 715 nm. Working distances were determined from the fit of equation 4 (red line) to the relative irradiance data (S/S_{mon}, black squares) as a function of sphere source position. Residuals to the fit are shown at the top of each subpanel.

A fit of equation 4 to the relative irradiance data is shown in Fig. 5 as the solid red line along with the fit residuals (top portion of each subpanel). The results of the fit for all three detectors are also summarized in Table 2, where m_1 and m_2 are fitting parameters and the aperture radii are known constants. For all three detectors the fit quality is good. The residuals are approximately 3 orders of magnitude smaller than the base measurements and show there is no obvious bias or offset. Another indication is the R^2-value, which is 1 for the trap detector and PED #1 but was less than 1 for PED #2.

$$y = \frac{m_1}{((M_0 - m_2)^2 + r_s^2 + r_d^2)} \quad (4)$$

The main result from the inverse square law fit is the value of m_2 for each detector, which determines the working distance from the sphere source position used in the irradiance responsivity measurements (see below) and allows calculation of the irradiance correction factor (equation 3). An important contributor to the overall uncertainty of the irradiance responsivity measurement is the fitting uncertainty obtained for m_2. The fitting uncertainty achieved for these pyroelectric detectors is somewhat larger compared to conventional semiconductor-based devices, probably due to the small signal-to-noise possible with the pyroelectric detectors. Some improvements could probably be made if longer measurement times were used during the inverse square law measurements. Still, the fitting uncertainty of 0.04 % for PED #1 and 0.12 % for PED #2 shows that it is possible for this method to become competitive with conventional methods of absolute irradiance responsivity calibrations.

Table 2: Results of the fit of equation 4 to the inverse square law measurements for the trap detector and pyroelectric detectors

	Trap		PED #1		PED #2	
Parameter	Value	Fitting Uncertainty	Value	Fitting Uncertainty	Value	Fitting Uncertainty
m_1 / mm^2	36210	23.8	2022.5	2.84	2420.6	9.81
m_2 / mm	-794.8	0.112	-805.2	0.126	-806.8	0.369
R^2	1	N.A.	1	N.A.	0.9999	N.A.
d / mm	291.3	0.038 %	301.6	0.042 %	303.2	0.12 %

NOTE 1: The working distance, d, of each detector used in the irradiance responsivity measurements for PED #1 and PED #2 is determined from the sphere source position (z = -503.56 mm) and from the detector position, m_2, on the Z-axis translation stage.

NOTE 2: N.A. means Not Applicable

With the detector positions known, the absolute irradiance responsivity calibration for PED #1 and PED #2 was completed at select tie point wavelengths with the sphere source positioned at -503.56 mm on the z-axis scale. The results of the calibration using equations 2 and 3 are shown as the orange tie points in Fig. 6 for both pyroelectric detectors where the error bars represent the standard deviation of the mean for the irradiance responsivity measurement. These results are overlaid with the absorptance spectra fit curve (blue points) determined in section A, above, after converting to the irradiance responsivity scale. This was done according to equation 5, where $I(\lambda)$ and $R(\lambda)$ are the spectral irradiance responsivity and spectral reflectance, respectively, and the absorptance at the tie point wavelength, 1-$R(\lambda_{\text{tie point}})$, was interpolated from the curve that was fit to the absorptance data (Fig. 3, red curve). Equation 5 divides the absorptance spectrum by a constant equivalent to the ratio of the absorptance to the irradiance responsivity at the chosen tie point wavelength. As mentioned earlier, this method assumes that the spectral irradiance responsivity is proportional to the absorptance spectrum, and that the relative absorptance spectra of the witness detectors are representative of that for PED #1 and PED #2 The inset graphs shown in Fig. 6 support these assumptions, where the variation in the irradiance responsivity with tie point wavelength follows closely the shape of the absorptance curve.

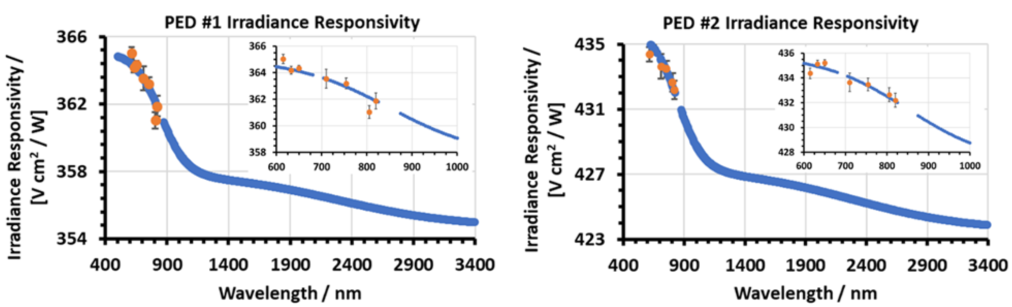

Fig. 6. Irradiance responsivity of pyroelectric detector #1 (left) and pyroelectric detector #2 (right) determined from witness sample absorptance (blue) and irradiance responsivity at tie points (orange) from a silicon trap detector. Inset: Shows an expanded view of the tie point region between 600 nm and 1000 nm, where the error bars indicate the measurement percent standard deviation of the mean.

$$I_{\text{DUT}}(\lambda) = \left[\frac{(1 - R(\lambda))}{1 - R(\lambda_{\text{tie point}})}\right] I_{trap}(\lambda_{\text{tie point}}) \quad (5)$$

For the data shown in Fig. 6 any of the tie points can be reasonably chosen such that it falls within the range between 500 nm and 900 nm where the silicon tunnel trap detector can be used with the lowest uncertainty. Choosing any tie point simply shifts the curve by a constant factor that would force the irradiance responsivity through the chosen tie point value. Alternatively, because the irradiance responsivity is proportional to the absorptance, the average ratio (irradiance responsivity to absorbance, i.e. $I_{trap}(\lambda_{\text{tie point}})/(1-R(\lambda_{\text{tie point}}))$ at the tie point wavelengths was used. This was done for the data in Figure 6 where the average ratio was 380.85 V cm^2/W ± 0.15 % and 454.76 V cm^2/W ± 0.09 % for PED #1 and PED #2, respectively, where the error is the percent standard deviation. By using all the tie points that were measured the overall uncertainty was expanded by the percent standard deviation of the constant factor arising from each tie point.

The total uncertainty budget is shown in Table 3 for both pyroelectric detectors as the relative standard uncertainty. Most of the typical SIRCUS calibration uncertainty components are comparatively small and included here for completeness. For example, the aperture areas (sphere and detector), amplifier gain (for the trap reference detector), wavelength, and geometry alignment only make minor contributions to the overall uncertainty. The irradiance calibration of the reference standard trap detector was completed directly from POWR with standard relative uncertainty of 0.05 %. If a working standard trap detector had been used this uncertainty component would be slightly higher at approximately 0.1 % which is the uncertainty associated from transferring the trap irradiance responsivity scale from the reference standard to the working standard on SIRCUS.

The major contributions to the uncertainty here arise from two parts, the irradiance measurement standard deviation from the pyroelectric detectors (due to the low signal-to-noise) and the uncertainty associated with the reflectance measurements. Low signal-to-noise not only increases the uncertainty in the irradiance responsivity calibration measurement, but also in determination of the distance correction factor in the inverse square law measurements. For the absorptance, the uncertainty comes from several main components. One, the uncertainty of the reflectance measurements from the individual witness samples ranged from 0.1 % to 0.36 % depending on the wavelength while, two, the point-to-point percent difference between the two witness samples was 0.05 % to 0.13 %. Fig. 7 shows the wavelength dependence of the uncertainty arising from the absorptance components as well as the wavelength dependence of the overall irradiance responsivity uncertainty (k=1). To generate a generalized responsivity curve, the reflectance data was fit as described above in Results/Discussion Section A. An additional uncertainty component was included to account for the quality of the fit to the experimental data and arises from the residuals to the fit. A relative contribution of 0.1 % was set for this component as most of the points in the wavelength range of interest have a residual of this value or less. Differences in the overall uncertainty magnitude for PED #1 and PED #2 largely arise from the difference in the distance uncertainty for the two pyroelectric detectors that resulted from the inverse square law measurements but are also somewhat offset by the percent standard deviation of the absorptance to irradiance responsivity ratio at the different tie points.

Table 3: Uncertainty Budget for Absolute Spectral Irradiance Responsivity of the Pyroelectric Detectors

	Relative Standard Uncertainty (*k*=1) / %	
Uncertainty Component	**PED #1**	**PED #2**
Irradiance Cal. Of Reference trap detector	0.05	0.05
Percent St.Dev of ratio tie points[1]	0.15	0.09
Distance[2]	0.114	0.256
Geometry Alignment	0.05	0.05
Amplifier Gain	N.A.	N.A.

Sphere Aperture	N.A.	N.A.
Reference detector Aperture	0.02	0.02
DUT Aperture (pyro)	N.A.	N.A.
Wavelength	0.01	0.01
Absorptance Percent St.Dev (Wavelength dependent)	0.1 to 0.36	0.1 to 0.36
Absorptance Fit Residual	0.1	0.1
Witness sample Absorptance %Difference (WL dependent)	0.05 to 0.13	0.05 to 0.13
Total Combined Uncertainty (*k*=1)	**0.28 (> 1000 nm) 0.36 (≈ 950 nm and < 900 nm) 0.44 (900 nm)**	**0.34 (> 1000 nm) 0.42 (≈ 950 nm and < 900 nm) 0.48 (900 nm)**

NOTE 1: Refers to the percent standard deviation from determining the ratio of irradiance responsivity to absorptance at each tie point.

NOTE 2: The distance uncertainty comprises the root-mean squared (RMS) percent error of the distance percent error for both the pyroelectric detector and the reference trap detector. The correction factor to the irradiance depends on the distance squared, which also results in an extra factor of 2 contribution to the irradiance responsivity uncertainty from the distance uncertainty.

It is also important to mention the wavelength dependence of the uncertainty across the wide spectral range covered by this irradiance scale. The major components giving rise to the wavelength dependence are from the uncertainty of the absorptance measurements and the slight point-to-point differences between the two witness samples. Fig. 7, top, shows the wavelength dependence of these uncertainty components while Fig. 7 bottom shows the overall uncertainty (*k*=1). The overall uncertainty has basically the same wavelength dependence as the absorptance uncertainty indicating this is the major contributing factor. The highest uncertainties occur around 900 nm with somewhat lower uncertainty of around 0.36 % and 0.41% for PED #1 and PED #2, respectively, below 900 nm and around 950 nm. Below approximately 950 nm, the lowest uncertainty calibrations directly from silicon trap detectors are available. The most significant results are for the range above approximately 950 nm. Above 1000 nm the uncertainties are lowest for both pyroelectric detectors and only slightly increase above 3000 nm (0.27 % to 0.29 % for PED #1 and 0.33 % to 0.35 % for PED #2), which is significantly lower than previously achieved in this range using conventional InGaAs or ex-InGaAs detectors. Although the uncertainties around 950 nm are somewhat higher, they are still competitive with conventional detectors.

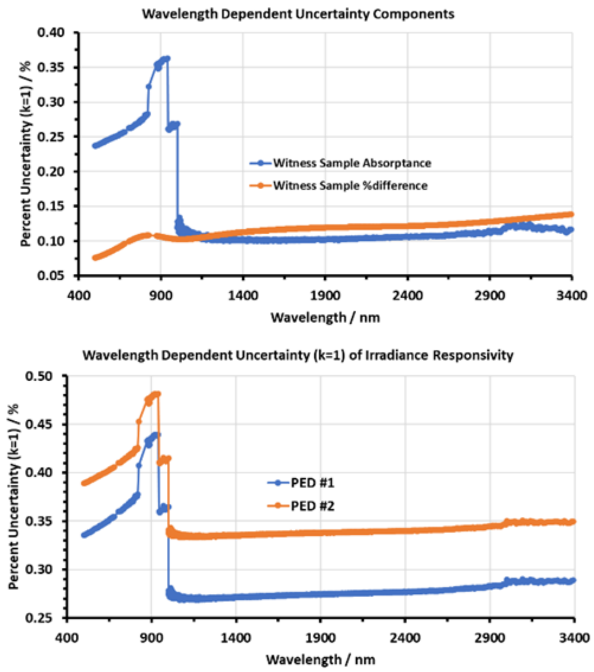

Fig. 7. Wavelength dependence of uncertainty components arising from the absorptance spectra (top) and the overall wavelength dependent uncertainty at k=1 (bottom) for the two pyroelectric detectors

Overall, the absolute irradiance responsivity of the two pyroelectric detectors above 1000 nm was found to be ≈ 0.28 % and ≈ 0.34 % for PED #1 and PED #2 respectively. Of course, there are some unquantifiable sources of uncertainty, especially concerning the use of a witness sample for reflectance measurements. First, only two witness samples were used to set the reproducibility of the reflectance. More samples are needed to establish statistical significance more clearly. Second, there is some chance the witness sample may not necessarily be equivalent to the absorptive layer in the real detectors PED #1 and PED #2. More certainty would be achieved if hemispherical reflectance measurements could be made on the real detectors, but this was prohibitive due to the detector housing. Furthermore, there is additional unquantifiable uncertainty for PED #2 for which the absorptive layer was not part of the same batch as the witness samples. Lastly, it should also be noted that the uncertainty budget, Table 3, does not include environmental effects on both the reference detector and the pyroelectric detectors. No evaluations of instrument performance characteristics such as temperature dependence, response linearity or temporal stability were performed.

4. Conclusions

An irradiance responsivity calibration was placed onto two pyroelectric detectors, utilizing a method that avoids a lock-in amplifier and the associated additional uncertainty components. The responsivity scale for each detector was established at standard uncertainty (k=1) of ≈ 0.28 % (> 1000 nm), 0.44 % (900 nm), and 0.36 % (≈ 950 nm and < 900 nm) for PED #1 and 0.34 % (> 1000 nm), 0.48 % (900 nm), and 0.42 % (≈ 950 nm and < 900 nm) for PED #2, covering the wavelength range 500 nm to 3400 nm. The uncertainties achieved are significantly lower than any known to be reported for irradiance responsivity calibrations above 1000 nm using laser-based techniques. Typically, InGaAs and extended-InGaAs detectors are used in the SWIR range but the main concern with these devices is the low spatial uniformity which leads to high uncertainty when the irradiance responsivity scale is transferred from power responsivity measurements. In addition, extended-InGaAs detectors are further limited due to low throughput, when an input sphere is used, and low temporal stability. Although InGaAs detectors have shown high enough spatial uniformity to be competitive with the technique described here at the 0.5 % level, extended-InGaAs detectors are still limited to several percent uncertainties or higher [13,5]. Therefore, the method described here offers significant improvement for extending the scale farther into the short-wave infrared from 900 nm to greater than 3000 nm with low uncertainties.

While less than 0.35 % (k=1) uncertainties were achieved in this report above 1000 nm, there still exists several opportunities for improvement and potential to achieve uncertainties approaching the 0.1 % level possible in the silicon range with trap detectors. There are two main sources which limited the uncertainty. One is the low signal-to-noise possible with low-NEP pyroelectric detectors. Two is the uncertainty associated with the reflectance measurements.

One way to offset the low signal-to-noise would be to average for longer time during the irradiance measurements (for both the inverse square law and responsivity measurements). Thirty-minute collections were used here for the irradiance responsivity measurements, but some improvements may have been possible for the fit uncertainty in the inverse square law measurements if more time-consuming scans had been completed. A second way would be to consider utilizing a collimated beam to increase the signal at the pyroelectric detector measurement plane. This would require some additional modifications to the irradiance measurements and the inverse square law would not be applicable, but the requirements on the distance measurements would also be less strict because the irradiance in a collimated beam will change less for a given error between the reference and DUT detector measurement planes. Overall, improvements to the signal-to-noise would not only give smaller measurement standard deviations but also allow for larger working distances to be used thereby reducing the uncertainty in the irradiance responsivity arising from the distance correction factor.

For the reflectance measurement uncertainty, there are also several factors to consider. One is that reflectance measurements on the actual pyroelectric detectors would eliminate uncertainty associated with various witness samples. Limitations in the detector housing and reflectance measurement geometry made such measurements not feasible for this work. Secondly, the reflectance of the black coating on each pyroelectric detector was found to be on the order of 5 %. This leads to a factor of ≈ 20 reduction in uncertainty when converted to absorptance, which for this study was around 0.1 % to 0.4 %. An improvement in this uncertainty could be made if a pyroelectric detector designed with an adsorptive coating with higher absorptance and lower reflectance was used [24].

In total, the pyroelectric detectors offer high potential for extension of irradiance/radiance responsivity scales further into the SWIR with low uncertainties on par with what is possible in the silicon range. Due to the broad spectral responsivity of the pyroelectric detectors, it is possible to conduct a scale transfer step from a silicon trap detector. This allows circumvention of the spatial nonuniformity problems detrimental to typical detectors when irradiance responsivity is determined from power responsivity (POWR) and aperture area. Nonetheless, there is still progress to be made towards achieving the lowest possible uncertainties with this method and further work to implement the improvements just described is currently underway.

5. Back Matter

Funding

This work was performed with funding from NASA Interagency Agreement No. NNG17JA08P.

Acknowledgements

We gratefully acknowledge our colleagues Steven W. Brown and George Eppeldauer for helpful discussions. We also acknowledge Stephen E. Maxwell for assistance with the Allan variance analysis.

Disclosures

The authors declare no conflicts of interest.

Data Availability

Data underlying the results presented in this paper are not publicly available at this time but may be obtained from the authors upon reasonable request.

Supplemental Document

See Supplement 1 for supporting content.

References

1. B. C. Johnson, H. Yoon, J. P. Rice, and A. C. Parr, "Chapter 1.2 - Principles of Optical Radiometry and Measurement Uncertainty," in *Experimental Methods in the Physical Sciences*, G. Zibordi, C. J. Donlon, and A. C. Parr, eds., Optical Radiometry for Ocean Climate Measurements (Academic Press, 2014), Vol. 47, pp. 13–67.
2. W. L. Wolfe, *Introduction to Radiometry* (SPIE Press Book, 1998), Vol. TT29.
3. F. Mélin and IOCCG, *Uncertainties in Ocean Colour Remote Sensing* (International Ocean Colour Coordinating Group (IOCCG), 2019).
4. N. Phojanamongkolkij, S. Kato, B. A. Wielicki, P. C. Taylor, and M. G. Mlynczak, "A Comparison of Climate Signal Trend Detection Uncertainty Analysis Methods," J. Climate **27**, 3363–3376 (2014).
5. J. T. Woodward, P.-S. Shaw, H. W. Yoon, Y. Zong, S. W. Brown, and K. R. Lykke, "Invited Article: Advances in tunable laser-based radiometric calibration applications at the National Institute of Standards and Technology, USA," Review of Scientific Instruments **89**, 091301 (2018).
6. S. W. Brown, G. P. Eppeldauer, and K. R. Lykke, "Facility for spectral irradiance and radiance responsivity calibrations using uniform sources," Appl. Opt., AO **45**, 8218–8237 (2006).
7. V. Ahtee, S. W. Brown, T. C. Larason, K. R. Lykke, E. Ikonen, and M. Noorma, "Comparison of absolute spectral irradiance responsivity measurement techniques using wavelength-tunable lasers," Appl. Opt., AO **46**, 4228–4236 (2007).
8. J. M. Houston and J. P. Rice, "NIST reference cryogenic radiometer designed for versatile performance," Metrologia **43**, S31–S35 (2006).
9. J. Fowler and M. Litorja, "Geometric area measurements of circular apertures for radiometry at NIST," Metrologia **40**, S9–S12 (2003).
10. K. D. Stock, R. Heine, and H. Hofer, "Spectral characterization of Ge trap detectors and photodiodes used as transfer standards," Metrologia **40**, S163–S166 (2003).
11. A. Lamminpää, M. Noorma, T. Hyyppä, F. Manoocheri, P. Kärhä, and E. Ikonen, "Characterization of germanium photodiodes and trap detector," Meas. Sci. Technol. **17**, 908–912 (2006).
12. M. López, H. Hofer, and S. Kück, "High accuracy measurement of the absolute spectral responsivity of Ge and InGaAs trap detectors by direct calibration against an electrically calibrated cryogenic radiometer in the near-infrared," Metrologia **43**, 508–514 (2006).
13. G. P. Eppeldauer, H. W. Yoon, Y. Zong, T. C. Larason, A. Smith, and M. Racz, "Radiometer standard for absolute responsivity calibrations from 950 nm to 1650 nm with 0.05% ($k = 2$) uncertainty," Metrologia **46**, S139–S145 (2009).
14. A. Carrasco-Sanz, F. Rodríguez-Barrios, P. Corredera, S. Martín-López, M. González-Herráez, and M. L. Hernanz, "An integrating sphere radiometer as a solution for high power calibrations in fibre optics," Metrologia **43**, S145–S150 (2006).
15. L. P. Boivin, "Properties of sphere radiometers suitable for high-accuracy cryogenic-radiometer-based calibrations in the near-infrared," Metrologia **37**, 273–278 (2000).
16. G. P. Eppeldauer, V. B. Podobedov, L. M. Hanssen, and C. C. Cooksey, "Low-NEP pyroelectric detectors for calibration of UV and IR sources and detectors," in *Sixteenth International Conference on Solid State Lighting and Led-Based Illumination Systems*, N. Dietz and I. T. Ferguson, eds. (Spie-Int Soc Optical Engineering, 2017), Vol. 10378, p. UNSP 1037809.
17. "Stanford Research Systems Application Note #3: About Lock-in Amplifiers," https://www.thinksrs.com/downloads/pdfs/applicationnotes/AboutLIAs.pdf, (n.d.).
18. V. B. Podobedov, G. P. Eppeldauer, L. M. Hanssen, and T. C. Larason, "Calibration of spectral responsivity of IR detectors in the range from 0.6 µm to 24 µm," in *Infrared Technology and Applications XLII* (International Society for Optics and Photonics, 2016), Vol. 9819, p. 98190P.
19. P. Y. Barnes, E. A. Early, and A. C. Parr, "Spectral reflectance," National Institute of Standards and Technology Special Publication **250–48**, 164 (1998).
20. "https://www.nist.gov/laboratories/tools-instruments/transfer-spectrophotometer," (n.d.).
21. L. Hanssen, S. Kaplan, and R. Datla, *Infrared Optical Properties of Materials* (National Institute of Standards and Technology, 2015), p. NIST SP 250-94.
22. L. M. Hanssen and S. Kaplan, "Infrared diffuse reflectance instrumentation and standards at NIST," Analytica Chimica Acta **380**, 289–302 (1999).

23. G. P. Eppeldauer, J. Zeng, H. W. Yoon, B. Wilthan, T. C. Larason, and L. M. Hanssen, "Extension of the NIST spectral responsivity scale to the infrared using improved-NEP pyroelectric detectors," Metrologia **46**, S155–S159 (2009).
24. S. P. Theocharous, E. Theocharous, and J. H. Lehman, "The evaluation of the performance of two pyroelectric detectors with vertically aligned multi-walled carbon nanotube coatings," Infrared Physics & Technology **55**, 299–305 (2012).